



Shell-Mediated Control of the Surface Chemistry in Highly Stoichiometric Magnetite Nanoparticles

Journal:	<i>Nanoscale</i>
Manuscript ID	NR-ART-03-2020-002069.R1
Article Type:	Paper
Date Submitted by the Author:	26-May-2020
Complete List of Authors:	Lavorato, Gabriel; INIFTA, ; Rubert, Aldo; INIFTA, Xing, Y. T. ; Universidade Federal Fluminense Instituto de Física Das, Raja; University of South Florida, Physics Robles-Garcia, Joshua; University of South Florida, Department of Physics Litterst, Fred Jochen; TU Braunschweig, Institute of Condensed Matter Physics, Saitovitch, Elisa; Centro Brasileiro de Pesquisas Físicas, Rua Dr. Xavier Sigaud 150, 22290-180 Rio de Janeiro, Brazil, Físicas Phan, Manh-Huong; University of South Florida, Physics Srikanth, Hariharan; University of South Florida, Physics Vericat, C; Instituto de Investigaciones Fisicoquímicas Teóricas y Aplicadas (INIFTA), Fonticelli, Mariano H.; The Research Institute of Theoretical and Applied Physical Chemistry (INIFTA), National University of La Plata- CONICET, Chemistry

ARTICLE

Shell-Mediated Control of the Surface Chemistry in Highly Stoichiometric Magnetite Nanoparticles

Received 00th January 20xx,
Accepted 00th January 20xx

DOI: 10.1039/x0xx00000x

Gabriel C. Lavorato,^{*a} Aldo A. Rubert^a, Yutao Xing,^b Raja Das,^{c,d} Joshua Robles,^e F. Jochen Litterst,^{f,g} Elisa Baggio-Saitovitch,^f Manh-Huong Phan,^e Hariharan Srikanth,^e Carolina Vericat,^a Mariano H. Fonticelli^{*a}

Magnetite (Fe₃O₄) nanoparticles are one of the most studied nanomaterials for different nanotechnological and biomedical applications. However, Fe₃O₄ nanomaterials gradually oxidize to maghemite (γ-Fe₂O₃) under conventional environmental conditions leading to changes in their functional properties that determine their performance in many applications. Here we propose a novel strategy to control the surface chemistry of monodisperse 12 nm magnetite nanoparticles by means of a 3 nm-thick Zn-ferrite epitaxial coating in core/shell nanostructures. We have carried out a combined Mössbauer spectroscopy, dc magnetometry, x-ray photoelectron spectroscopy and spatially-resolved electron energy loss spectroscopy study on iron oxide and Fe₃O₄/Zn_{0.6}Fe_{2.4}O₄ core/shell nanoparticles aged under ambient conditions for 6 months. Our results reveal that while the aged iron oxide nanoparticles consist of a mixture of γ-Fe₂O₃ and Fe₃O₄, the Zn-ferrite-coating preserves a highly stoichiometric Fe₃O₄ core. Therefore, the aged core/shell nanoparticles present a sharp Verwey transition, an increased saturation magnetization and the possibility of tuning the effective anisotropy through the exchange-coupling at the core/shell interface. The inhibition of the oxidation of the Fe₃O₄ cores can be accounted for in terms of the chemical nature of the shell layer and an epitaxial crystal symmetry matching between the core and the shell.

Introduction

Iron oxide nanomaterials are being proposed for multiple applications ranging from biomedicine to spintronics. Magnetite (Fe₃O₄) and maghemite (γ-Fe₂O₃) have been approved, for example, as agents for medical imaging, magnetic fluid hyperthermia and drug delivery systems^{1–5}. At the same time, self-assembled Fe₃O₄ nanoparticles (NPs) and thin films have attracted attention in the field of spin-dependent electronic transport for the design of novel magnetoresistive devices^{6–13}, in which the half-metallic nature and the spin-polarization of Fe₃O₄ play a central role. However, most

nanomaterials contain variable amounts of Fe₃O₄ and γ-Fe₂O₃ due to the relatively easy oxidation of Fe²⁺ to Fe³⁺ under environmental conditions^{14–17}. Such process, usually undesired, is a key factor to control the materials' properties, as it decreases both the overall magnetic moment and the magnetocrystalline anisotropy^{16,18} and leads to a decreased electrical conductivity¹⁹. In addition, the chemical stability of Fe₃O₄ NPs is relevant in the biomedical field as they can play an important role in the cellular oxidative stress and toxicity and also display peroxidase-like catalytic activity through heterogeneous Fenton reactions^{20–23}.

Magnetite crystallizes in an inverse spinel structure where 1/3 of Fe cations are in Fe²⁺ state and 2/3 in Fe³⁺ state. Fe²⁺ cations mostly occupy octahedral sites (*Oh*), while Fe³⁺ are equally distributed between tetrahedral (*Td*) and *Oh* sites: (Fe³⁺)_{*Td*}[Fe²⁺Fe³⁺]_{*Oh*}O₄. The uncompensated magnetic moment resulting from the antiferromagnetic interaction between moments in *Td* and *Oh* sites is responsible for a ferrimagnetic ordering and a bulk saturation magnetization of 98 emu/g at low temperature¹⁹. Due to the electron hopping between Fe²⁺ and Fe³⁺, Fe₃O₄ exhibits a half-metallic nature with a partially filled spin-polarized band¹⁹. A charge-ordered insulating state is observed below the Verwey transition at T_V ≈ 120 K²⁴, which is highly sensitive to the stoichiometry, crystallinity and size^{25–27}. In Fe₃O₄ NPs and thin films, T_V is typically shifted to lower values and is no longer observed for NPs smaller than ≈ 8 nm²⁸ or very thin films²⁵.

Although hematite (α-Fe₂O₃) is the thermodynamically most stable iron oxide phase and Fe₃O₄ is oxidized to hematite at

^a Instituto de Investigaciones Físicoquímicas Teóricas y Aplicadas (INIFTA), Universidad Nacional de La Plata – CONICET, 1900 La Plata, Buenos Aires, Argentina.

^b Laboratório de Microscopia Eletrônica de Alta Resolução, Centro de Caracterização Avançada para Indústria de Petróleo (LaMAR/CAIPE), Universidade Federal Fluminense, 24210-346, Niterói, RJ, Brasil.

^c Faculty of Materials Science and Engineering and Phenikaa Institute for Advanced Study (PIAS), Phenikaa University, Hanoi, 10000, Vietnam.

^d Phenikaa Research and Technology Institute (PRATI), A&A Green Phoenix Group, 167 Hoang Ngan, Hanoi 10000, Vietnam.

^e Department of Physics, University of South Florida, 33620 Tampa, FL, United States.

^f Centro Brasileiro de Pesquisas Físicas, 22290-180 Rio de Janeiro, RJ, Brasil.

^g Institut für Physik der Kondensierten Materie, Technische Universität Braunschweig, 38106 Braunschweig, Germany.

*gclavorato@inifta.unlp.edu.ar; mfonti@inifta.unlp.edu.ar

† Electronic Supplementary Information (ESI) available: [Additional TEM images, X-ray diffractograms, analysis of the Mössbauer spectroscopy and dc magnetometry data, simulations on the power losses, evaluation of the Fe₃O₄ oxidation process]. See DOI: 10.1039/x0xx00000x

temperatures above 400 °C²⁹, at room temperature Fe₃O₄ transforms within months into γ -Fe₂O₃ in a topotaxial oxidation process^{14,30,31} according to $2\text{Fe}_3\text{O}_4 + \frac{1}{2}\text{O}_2 \rightarrow 3\text{Fe}_2\text{O}_3$. γ -Fe₂O₃ retains a spinel structure where Fe³⁺ is distributed in both sites: (Fe³⁺)_{Td}[Fe³⁺_{5/3}□_{1/3}]_{Oh}O₄, leaving additional vacancies (□) in Oh sites. As a result, the low temperature magnetization is 82 emu/g, the bulk anisotropy constant is reduced compared to magnetite and, due to the absence of electron hopping, γ -Fe₂O₃ is an electrical insulator^{19,32}.

The earliest reports dealing with the mechanisms underlying the oxidation of magnetite to maghemite pointed to the outward diffusion of Fe cations³⁰. It is accepted that in such process adsorbed oxygen is ionized by the electrons arising from the oxidation of Fe²⁺ to Fe³⁺, providing an iron concentration gradient that drives the diffusion of additional cations^{14,30}. Several authors have shown that NPs, due to their large surface-to-volume ratios, easily form maghemite-magnetite mixtures^{14,33–35}; however, it is less clear if those mixtures consist of a magnetite core with a uniform maghemite surface layer^{33,34} or they rather form non-stoichiometric oxides^{27,35,36}. In addition, the values of Fe cation diffusivities vary strongly among different reports, suggesting that there may be additional factors, such as crystallinity, strain or impurities that can determine the kinetics of the transport processes^{14,35,37–39}.

The aforementioned background shows that the magnetite oxidation process is of fundamental importance in the design and application of nanomaterials and a great effort has been made to preserve the chemical stability of iron oxide NPs. For example, although a SiO₂ coating layer⁴⁰ has demonstrated to be effective to transfer the NPs into aqueous media and to prevent their aggregation by decreasing the interparticle dipolar interactions^{41,42}, several reports show that the Verwey transition is suppressed after the deposition of the SiO₂ layer on Fe₃O₄ cores^{43–46}. The SiO₂ shell, being non-magnetic, is also detrimental to the magnetic properties since it decreases the overall magnetization of the system⁴⁷. In this context, an effective strategy to obtain a chemically stable stoichiometric magnetite while preserving the magnetic properties of the material is highly desirable.

Here, we took an advantage from the epitaxial growth of different ferrites with similar crystal lattices in core/shell structures⁴⁸ to synthesize Fe₃O₄/Zn_{0.6}Fe_{2.4}O₄ core/shell NPs. We demonstrate that the stoichiometry of the Fe₃O₄ core is preserved by the Zn_{0.6}Fe_{2.4}O₄ shell after 6 months of environmental aging, while bare cores lead to the partial formation of γ -Fe₂O₃. The ferrite layer also provides an enhanced overall magnetization and the possibility to control the effective anisotropy through the exchange-coupling at the core/shell interface.

Materials and methods

Synthetic procedures

Chemicals. Fe (III) acetylacetonate (Fe(acac)₃, 99%) was purchased from Acros. Zn (II) acetylacetonate hydrate

(Zn(acac)₂), Oleic acid (OA, 90 %), 1,2-Hexadecanediol (HDD, 90%), Oleylamine (OAm, 70%), Benzylether (98%), Ethanol (99.9%) and Hexane (99%) were purchased from Sigma-Aldrich. All reagents were used as received without any further modifications.

Synthesis of Fe₃O₄ cores. Fe₃O₄ cores were synthesized by the seed-mediated thermal decomposition of Fe(acac)₃ with OA, OAm and HDD in benzyl ether as proposed by Sun et al.⁴⁹. We decided to employ this method because it yields single-crystalline Fe₃O₄ NPs free of structural defects^{48,50} that would complicate the interpretation of the results or would require additional synthetic steps⁵¹. In a typical process, Fe(acac)₃ (2 mmol) were mixed with HDD (10 mmol), OA (6 mmol) and OAm (6 mmol) in benzyl ether (20 mL). The liquid was magnetically stirred during the whole process under a N₂ atmosphere. After being degassed for 30 min at 110 °C, the mixture was heated to 200 °C (heating rate 10 °C min⁻¹) and kept at that temperature for 120 min; afterwards, the temperature was raised up to 300 °C (heating rate 20 °C min⁻¹) for 60 min and subsequently cooled by removing the heating source. The NPs (ca. 6 nm diameter) were precipitated twice by addition of hexane:ethanol 1:8 and centrifugation (2800 rcf). To grow larger particles, the obtained NPs were employed as seeds in a seed-mediated process. In a typical synthesis, Fe(acac)₃ (2 mmol) were mixed with HDD (10 mmol), OA (3 mmol) and OAm (3 mmol) in benzyl ether (20 mL); after dissolving the reagents at 70 °C, 100 mg of 6 nm NPs dispersed in 4 mL of hexane were added and the mixture was degassed at 105 °C to remove the water and the hexane. Then, the heating procedure was repeated with slightly different times (60 min at 200 °C and 30 min at 300 °C). The obtained particles, ca. 8 nm, were used again as seeds by repeating the procedure above to obtain larger NPs with a ca. 12 nm diameter. A fraction of the 12 nm Fe₃O₄ NPs was separated for further characterization and the rest was used as seeds for the fabrication of core/shell NPs.

Synthesis of core/shell NPs. The 12 nm Fe₃O₄ cores were used as seeds for the fabrication of Fe₃O₄/Zn_{0.6}Fe_{2.4}O₄ core/shell NPs. In a typical process, Fe(acac)₃ (1 mmol) and Zn(acac)₂ (0.5 mmol) were mixed with HDD (10 mmol), OA (6 mmol) and OAm (6 mmol) in benzyl ether (20 mL) and, after dissolving the reagents at 70 °C, 100 mg of 12 nm Fe₃O₄ cores dispersed in 4 mL of hexane were added and the mixture was degassed for 30 min at 105 °C. Then, the system was heated directly to 300 °C (heating rate 20 °C min⁻¹) and kept at that temperature for 60 min, while maintaining continuous N₂ bubbling and magnetic stirring. A 1:2 Zn(acac)₂:Fe(acac)₃ molar ratio was employed to obtain a Zn_{0.6}Fe_{2.4}O₄ composition in the shell since the effective Zn:Fe molar ratio in the shell is expected to be lower than the precursors ratio due to differences in the reaction mechanism of metal acetylacetonates^{52,53}. The obtained NPs were washed twice with a hexane:ethanol 1:8 mixture and are easily dispersed in hexane or other non-polar solvents. The hydrophobic nature of both samples is determined by the capping layer resulting from the synthesis process, which is mostly composed by oleate molecules whose affinity to the metal oxide is larger compared to amines⁵⁴. For our particular

size range, the capping layer density can be estimated to be ≈ 2 ligands/nm² according to previous reports^{55–57}.

Environmental aging. Both core and core/shell samples were dried and stored under air atmosphere at room temperature. Unless indicated, the structural and magnetic characterization experiments were performed 6 months after their synthesis.

Characterization methods

X-ray diffraction experiments were conducted in a X'Pert PRO equipment (Philips, PANalytical) with a Bragg-Brentano geometry by measuring the dried powder in a low-background sample holder. 2θ angles were scanned between 25 and 70 ° with a step size of 0.017 ° while any possible systematic errors were checked with a Si standard.

The size of the NPs was evaluated by measuring at least 200 NPs of each sample from transmission electron microscopy (TEM) images obtained in a FEI Morgagni 268D microscope. The structure, morphology and electron energy loss spectra of the NPs were studied in a JEOL JEM 2100F microscope by scanning transmission electron microscopy (STEM) and high-resolution transmission electron microscopy (HRTEM) images. The Zn and Fe elemental analysis was evaluated by acquiring energy-dispersive X-ray spectroscopy (EDS) images in STEM mode in a FEI TALOS F200X G2 microscope. In every case, the samples were prepared by drying 10 μ L of a diluted dispersion of the NPs on a C-covered Cu grid.

The histograms from the size analysis were fitted with a lognormal function $f(d) = (\sqrt{2\pi}\sigma d)^{-1} e^{-\frac{(\ln d/d_0)^2}{2\sigma^2}}$, where d_0 is the median diameter and σ is the deviation. The standard deviation (SD) obtained from the fit is therefore given by $SD = d_0 e^{\sigma^2/2} \sqrt{e^{\sigma^2} - 1}$. As a result, the reported sizes are given in the form $d_0(SD)$ nm⁵⁸. Line profiles of the Fe and Zn EDS intensities were obtained by means of the ImageJ software⁵⁹ by averaging the recorded intensity of the spectrum image along a line (2 nm width) from the surface of a single core/shell NP. Simulations of the intensities for a core/shell NP were performed by considering the projected volume of a spherical particle in a plane perpendicular to the electron beam (an overall diameter of 17.2 nm and a core diameter of 12.1 nm were employed). A perfectly sharp interface and a 1:0.8 relative intensity of Fe in the core and Fe in the shell were also considered in the simulations.

The overall amount of Fe and Zn in the samples was evaluated in an inductively-coupled plasma mass spectrometer (ICP-MS, Agilent 7500). Around 2 mg of each sample were digested in ultrapure HNO₃ and diluted for the experiments. The analysis of the results for the core/shell NPs confirms that the shell composition is close to Zn_{0.6}Fe_{2.4}O₄.

X-ray photoelectron spectroscopy (XPS) measurements were done with a non-monochromatic Al K α source at 1486.6 eV (XR50, Specs GmbH) and a hemispherical electron energy analyzer (PHOIBOS 100, Specs GmbH) operating either at 10 or 40 eV pass energy. A two-point calibration of the energy scale was performed using sputtered cleaned gold (Au 4f_{7/2}, binding energy=84.00 eV) and copper (Cu 2p_{3/2}, binding energy=932.67 eV) samples. NPs' samples were prepared by drop casting

purified NP dispersions on carbon substrates (Ted Pella, Inc). Spectra were analyzed with CasaXPS v2.3.14 software. Shirley-type backgrounds were used in the fitting procedure of the high-resolution spectra. For quantitative analysis, peak intensities were corrected by the corresponding Relative Sensitivity Factors. The fitting of the Fe 2p peaks was carried out using a free spin-orbit splitting between 13.2 and 13.9 eV and a branching ratio of 0.5. Analysis of the Fe3s signals served as a guide to define the peak fitting criteria.

Hysteresis loops were measured in a PPMS (Quantum Design) equipped with a vibrating sample magnetometer with fields up to ± 50 kOe at 5 K and 300 K. Magnetization versus temperature zero-field-cooled (ZFC) and field-cooled (FC) curves were obtained between 5 K and 330 K and were both measured during warming with an applied field of 50 Oe. Samples were dried and pressed into gelatin capsules for the measurements. The magnetization values are referred to the total mass of the NPs, which includes a small contribution (≈ 5 –8 wt%) of oleate molecules from the capping. Room-temperature ⁵⁷Fe Mössbauer spectra were recorded in transmission geometry using a ⁵⁷Co:Rh source moving in a sinusoidal mode. Dried powders of the NP samples were pressed into thin discs for measurements and isomer shifts are reported relative to α -Fe at room temperature.

Results and discussion

The chemical stability of iron oxides determines to a great extent the functional properties of NPs and our work explores the passivation of magnetite cores by a Zn-ferrite layer in core/shell Fe₃O₄/Zn_{0.6}Fe_{2.4}O₄ heterostructures. We chose Zn-ferrite since it has the same crystal structure with a lattice parameter close to that of magnetite, an excellent crystal symmetry matching between core and shell and a minimum epitaxial strain, while providing a good biocompatibility, in contrast to other ferrites⁶⁰. We studied by means of different experimental techniques the bare iron oxide cores and the core/shell NPs after a 6-month aging of the dry powders in air at room temperature. It is worth noting that, for consistency, *bare cores* refer to iron oxide particles solely protected by the capping agent from the synthesis, which are the same that were used as seeds in the synthesis of the core/shell heterostructures.

Figure 1 shows representative TEM images of both samples, while additional images are shown in the Supporting Information section. Size distribution histograms and lognormal fits reveal that the median size is 12.1(1.3) nm for the cores and 17.2(1.8) nm for the core/shell NPs, indicating a narrow size distribution and a 2.6(3) nm-thick shell. The epitaxial growth of the Zn ferrite is confirmed by HRTEM images and the associated FFT that evidence an excellent crystallinity. HRTEM images also show that the nanocrystals are mostly truncated octahedra with {111} facets, as expected due to the presence of the long chain diol which promotes the growth of {100} and {110} planes⁶¹. The core/shell morphology of the samples is further confirmed by EDS results, as shown in Figure 1f, which reveal a uniform ≈ 3 nm-thick Zn-rich layer. The Fe and Zn EDS signals along a single

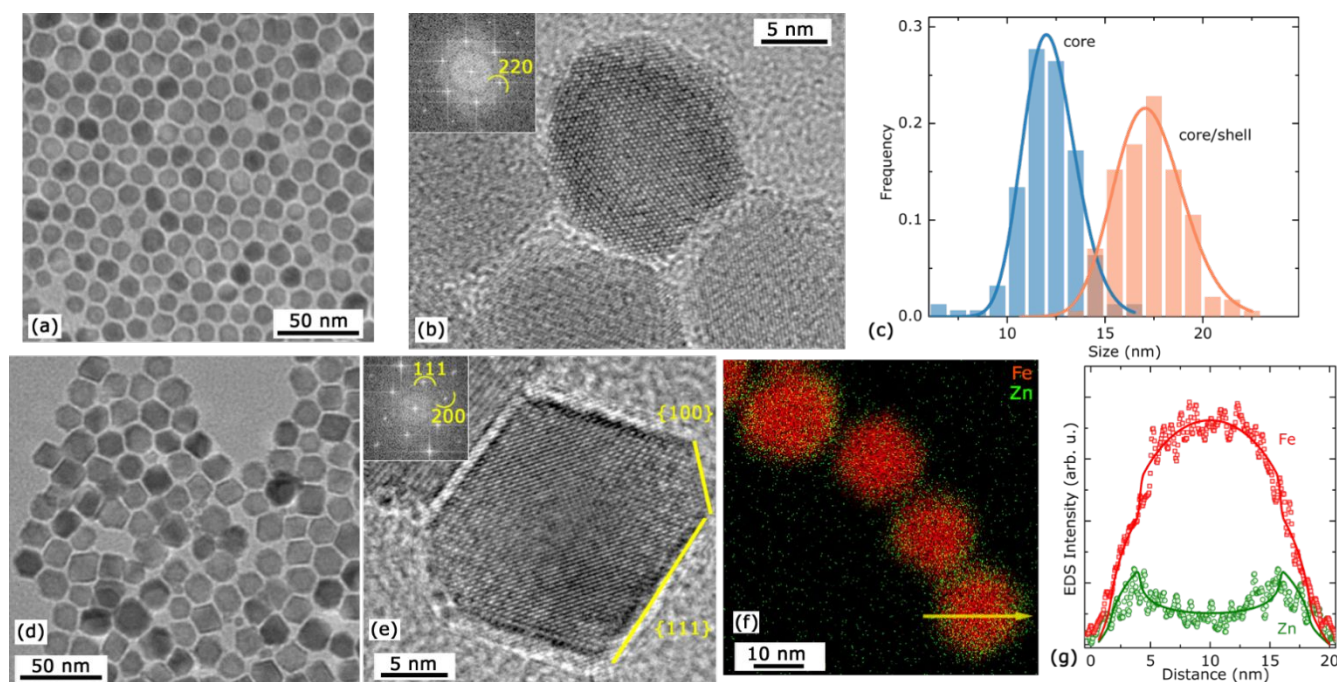


Figure 1 Summary of the TEM characterization. (a) TEM and (b) HRTEM images for iron oxide cores, (c) size histograms and lognormal fits, (d) TEM and (e) HRTEM images for $\text{Fe}_3\text{O}_4/\text{Zn}_{0.6}\text{Fe}_{2.4}\text{O}_4$ core/shell NPs. (f) Fe and Zn EDS elemental mapping for the core/shell NPs and (g) Intensity of the Fe and Zn EDS signals as a function of the distance from the NP surface along the line indicated in (f); solid lines indicate the simulations for core/shell spherical NPs with a perfectly sharp interface (the reader is referred to the text for more details). Insets in panels (b) and (e) show the FFT of the associated HRTEM images.

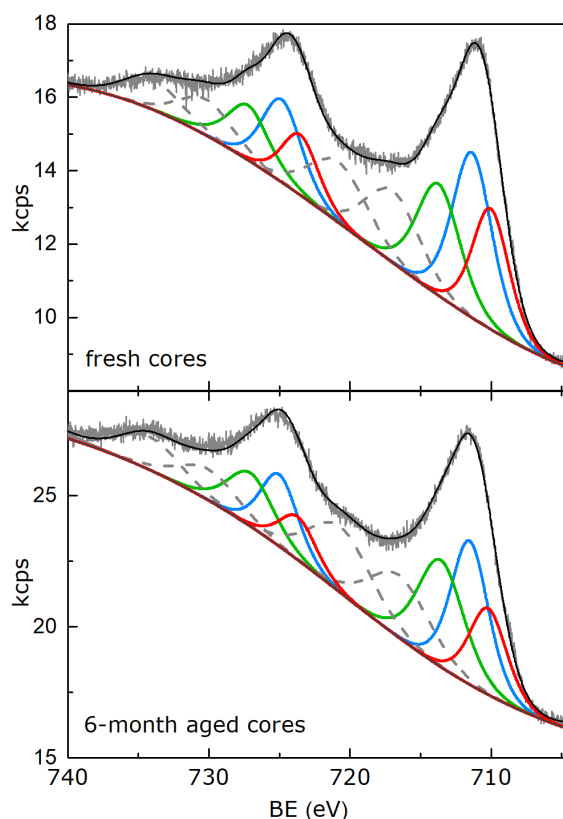


Figure 2 High resolution Fe 2p XPS spectra of fresh and 6-month aged iron oxide bare cores. Solid lines indicate peaks assigned to Fe^{2+} in octahedral sites (red), Fe^{3+} in octahedral sites (blue) and Fe^{3+} in tetrahedral sites (green), while gray dashed lines are mostly assigned to shake-up satellites.

NP are presented in Figure 1g together with the simulated intensities expected for a 17.2 nm core/shell NP with a 12.1 nm core and a perfectly sharp interface (additional details on the profile analysis procedure are reported in the Experimental Section). A good agreement between the simulations and the experiments suggests that the interface between the core and shell is abrupt and diffusion at the interface is not significant even after 6 months of shelf life.

Fe 2p X-ray photoelectron spectra of freshly-prepared and 6-month aged iron oxide cores are shown in Figure 2. The use of broad peak shapes during the fitting procedure is not useful for the identification of mixtures of iron phases due to the spectral overlap of most Fe^{3+} compounds which show similar binding energies but vary in peak shape and satellite intensity⁶². The fitting procedure was performed using the lowest number of peaks (FWHM about 3eV) for the achieved resolution. Both samples show three main peaks for Fe $2p_{3/2}$ signals and two more signals which can be mostly assigned to shake-up satellites (gray dashed peaks). Fe $2p_{3/2}$ signals with peak maxima at 710.1, 711.5 and 713.8 eV can be assigned to Fe^{2+} in octahedral sites (red solid line), Fe^{3+} in octahedral sites (blue solid line) and Fe^{3+} in tetrahedral sites (green solid line), respectively^{63,64}. For both samples, iron oxidation states ratios ($\text{Fe}^{2+}/\text{Fe}^{3+}$) can be calculated from the peak areas, resulting in $\text{Fe}^{2+}/\text{Fe}^{3+} = 0.39$ for fresh bare cores and 0.31 for 6-month aged bare cores. This clearly shows that the Fe^{2+} contribution decreases as a result of the environmental aging process.

After confirming the environmental oxidation of iron oxide cores, we decided to study the structural and magnetic properties of bare cores and core/shell NPs following the 6-

month aging. From X-ray diffraction measurements a single cubic spinel structure is observed for all samples; however, the aged bare cores exhibit a lattice parameter intermediate between the values reported for Fe_3O_4 and $\gamma\text{-Fe}_2\text{O}_3$ ³² (Figure S2). A more careful estimation of the degree of oxidation by XRD is difficult since peak broadening due to the formation of maghemite can complicate the comparison of different samples³⁴. On the other hand, the lattice parameter for the aged core/shell NPs is between the expected value for bulk Fe_3O_4 and Zn-ferrite. At this point it is worth noting that the composition of the shell was set to $\text{Zn}_{0.6}\text{Fe}_{2.4}\text{O}_4$ in order to minimize the lattice mismatch between the core and the shell. Such composition was verified by ICP-MS and is achieved by adjusting the molar ratios of Zn and Fe acetylacetonates, as described in the experimental section. The lattice parameter of the shell, estimated from Vegard's rule⁶⁵, is expected to be only

and the outer part of the core/shell NPs, as shown in Figure 3. The most common strategies involve either the comparison of the $\text{Fe}_{\text{L}3}$ edge energy, which is shifted to lower values when the Fe^{2+} content increases, or the $\text{Fe}_{\text{L}3}/\text{Fe}_{\text{L}2}$ intensity ratio, which increases for larger Fe^{3+} contents^{68,69}. In Figure 3b the $\text{Fe}_{\text{L}3}/\text{Fe}_{\text{L}2}$ ratio is plotted as a function of the distance along a single core/shell NP. While the inner part shows a $\text{Fe}_{\text{L}3}/\text{Fe}_{\text{L}2}$ ratio around 4.7(2), this increases above 5 for the outer part of the particle. This result is consistent with the shell thickness determined by EDS and indicates the existence of a sharp interface between the core and the shell that separates a Fe^{2+} -containing magnetite core^{68,69} from the shell dominated by the Fe^{3+} contribution, even after environmental aging of the core/shell NPs.

Once the environmental aging of iron oxide cores was confirmed by XPS and the existence of a $\text{Fe}^{2+}/\text{Fe}^{3+}$ interface in the aged core/shell samples determined by EELS, we turned our attention to the evaluation of the overall iron oxidation state and the cation occupancy. To this end, we measured room temperature Mössbauer spectra of the 6-month aged samples, which are shown in Figure 4. Mössbauer spectra of ferrites are typically analyzed by considering the contribution of different subspectra corresponding to Fe cations either in *Oh* or in *Td* sites. In the case of Fe_3O_4 , two subspectra are expected above the Verwey transition: one from $\text{Fe}^{2+}\text{-Fe}^{3+}$ in *Oh* sites and another associated to Fe^{3+} in *Td* sites, which differ in their isomeric shift and hyperfine field^{18,36,70,71}. In contrast, the absence of Fe^{2+} in $\gamma\text{-Fe}_2\text{O}_3$ yields a lower average isomeric shift, which is a good indicator of the magnetite-maghemite fraction in the sample⁷². In our case, the iron oxide aged cores show a spectrum formed by sextets with broadly distributed hyperfine fields, and the separation of the different subspectra is not unambiguous. This cannot be attributed to pure magnetite^{72,73}, but to a mixture of magnetite and maghemite. A good fit to the experimental data (fitting parameters can be found in Table S1) was achieved with three magnetic sextet patterns (S1-S3) with Gaussian broadened hyperfine fields that are ascribed to relaxational dynamics of the NP moments. While the three patterns have no direct interpretation, this fit allows determining the center of gravity of the total spectral area, *i.e.* the average isomer shift of magnetite and maghemite contributions as described in ref.⁷². We obtain 0.43(2) mm/s for this shift, which is between the values expected for maghemite and magnetite, 0.35 and 0.53 mm/s respectively^{36,72}, suggesting that the aged cores are formed by a $\approx 55\%$ of maghemite, in agreement with the results from XRD.

On the other hand, a good fit to the core/shell spectrum could be achieved using 5 sextet subspectra associated with Fe in *Td* and *Oh* sites of the magnetite core, Fe^{3+} in *Td* and *Oh* sites in the shell and an additional small contribution ($<3\%$) by a divalent iron species (for clarity, not shown in the graph). The shell sites reveal broadened magnetic patterns that were approached by Gaussian broadened magnetic hyperfine fields. When compared to the spectra of the bare cores, the spectra of the magnetite sites are considerably less broadened, indicating that the relaxational broadening seen for the bare cores is

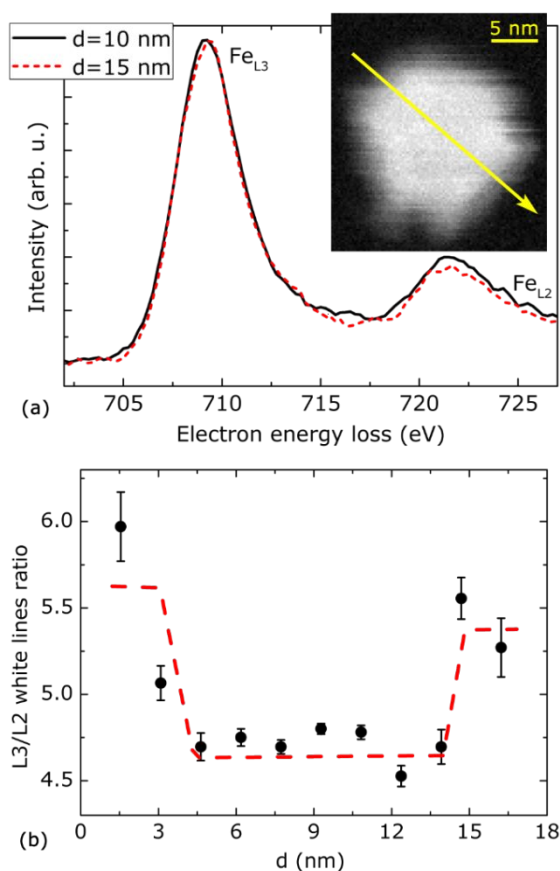


Figure 3 (a) Typical normalized electron energy loss spectra of $\text{Fe}_{\text{L}2,3}$ at different positions of a $\text{Fe}_3\text{O}_4/\text{Zn}_{0.6}\text{Fe}_{2.4}\text{O}_4$ core/shell NP. Inset: associated full-spectrum STEM image. (b) Plot showing the typical change in the $\text{Fe}_{\text{L}3}/\text{Fe}_{\text{L}2}$ intensities ratio for the line scan in the core/shell NPs.

0.35% larger than the magnetite reference value, confirming an excellent matching between core and shell lattices.

Next we focused on investigating the spatial variation of the Fe oxidation state in the core/shell samples by electron energy loss spectroscopy (EELS), which gives valuable information since $\text{Fe}_{\text{L}2,3}$ white lines depend on the iron oxidation state^{66,67}. To this end, we acquired full-spectrum STEM images that allowed for comparison of the electron energy loss spectra from the inner

suppressed due to the magnetization of the shell. The spectral area ratios between magnetite *Td* and *Oh* sites were kept fixed to the ideal value of 1:2. The isomer shifts of the trivalent magnetite *Td* sites and the intermediate valence *Oh* sites were fixed to the literature values⁷², quadrupole splittings were less than 0.02 mm/s. The hyperfine parameters for the core and shell sites derived from our fits are given in Table S2 in the Supporting Information section. According to the fitted results, 43(5) % of the aged core/shell NPs are formed by a stoichiometric Fe₃O₄, in good agreement with the core volume from the structural characterization, which was estimated to be around 35 %. In addition, our results indicate that 78(5) % of the Fe cations in the shell are located in *Oh* sites, pointing to a strong preference of Zn²⁺ cations to the *Th* sites of the ferrite shell. Even if this was already expected from previous reports on single-phase bulk ferrites^{74–76} and NPs^{77,78}, it still remained to be confirmed for core/shell NPs, where the shell-phase epitaxial growth on the magnetite cores may induce distortions in the cation occupancy⁷⁹, leading to unexpected magnetic properties, as was shown *e.g.* in thin films⁸⁰.

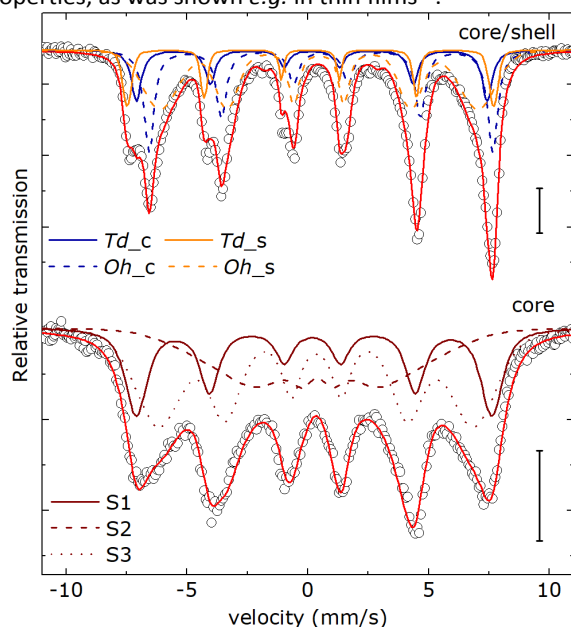


Figure 4 Room temperature Mössbauer spectra for 6 month-aged iron oxide cores (lower spectrum) and core/shell Fe₃O₄/Zn_{0.6}Fe_{2.4}O₄ NPs (upper spectrum). Lines indicate the fits associated with different sextets. *Td_c*, *Oh_c*, *Td_s* and *Oh_s* subspectra are associated to iron in tetrahedral (*Td*) and octahedral (*Oh*) sites in core and shell, respectively. The bars indicate a relative transmission of 1%.

A further evidence of an increased chemical stability of the magnetite core due to the presence of a ferrite shell is provided by magnetometry. Figure 5 shows the temperature dependence of the magnetization. While the ZFC-FC magnetization curves for the aged cores reveal a broad rise of M_{ZFC} with temperature, the aged core/shell NPs show a remarkably sharp Verwey transition at $T_V=108(1)$ K. Such value can be compared to that reported by Hyeon and colleagues²⁸, who evaluated the size-dependence of the Verwey transition and showed that highly crystalline 10–15 nm NPs present a T_V around 105–110 K. It is important to note that in ref. 28 the samples were kept under

inert atmosphere for the entire characterization process while our core/shell NPs have been aged for 6 months in air. As the Verwey transition is highly sensitive to the Fe₃O₄ stoichiometry²⁴, this represents a strong indication that the shell layer is preserving the Fe²⁺ in the iron oxide core upon environmental aging and that there is no diffusion of Zn into the core, in agreement with the structural characterization. In addition, T_V is found to be unchanged within the 6 month-aging period and, notably, we did not observe any further stabilization of the transition towards the bulk value, unlike recent observations in strained epitaxial thin film bilayers^{81,82}.

The comparison of the saturation magnetization values for fresh and aged NPs at room-temperature is shown in Table 1. The iron oxide cores exhibit a 12% decrease in the magnetization value, while it is almost unaltered for the core/shell sample, supporting the hypothesis of the passivation effects of the Zn-ferrite coating on the Fe₃O₄ cores. The hysteresis loops of both (aged) samples are shown in Figure 6. The single-reversal process observed for hybrid NPs is in agreement with a rigid coupling between the Fe₃O₄ and the Zn-ferrite shell^{81,83} as a result of the core/shell nature of the samples. A significantly larger M_S is evidenced for the core/shell NPs, particularly at 5 K: 109.2 emu/g against 65.1 emu/g. While the latter value is lower than the expected value for bulk maghemite (83 emu/g)³², the core/shell magnetization is even larger than the bulk magnetite reference (98 emu/g)¹⁹.

Table 1 Room temperature saturation magnetization (obtained at 10 kOe) for fresh and 6-month aged iron oxide cores and Fe₃O₄/Zn_{0.6}Fe_{2.4}O₄ core/shell nanoparticles.

Sample	M_S (emu/g)	
	Fresh	Aged
Core	66.8(7)	58.7(6)
Core/shell	80.6(7)	79.9(7)

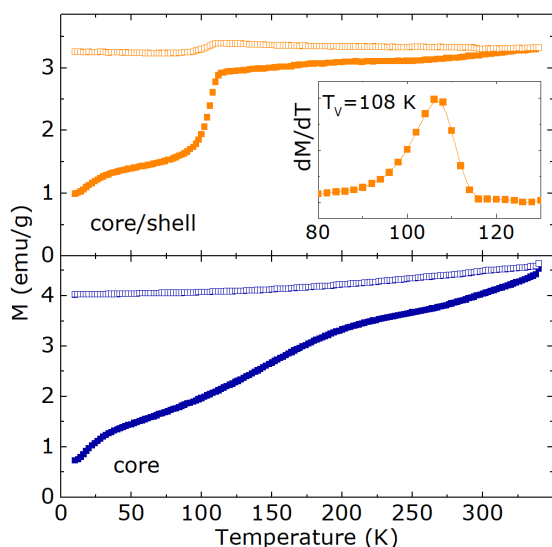


Figure 5 Zero-field cooled (ZFC, full symbols) and field-cooled (FC, open symbols) temperature dependence of the magnetization for 6 month-aged cores and core/shell NPs. The inset shows the derivative of the ZFC curve and the Verwey transition temperature.

Since we have clear evidence that the core/shell NPs retain a stoichiometric magnetite core, we can estimate the magnetization contribution of the shell layer by considering the core and shell volume fractions estimated by TEM or Mössbauer spectroscopy and the bulk reference magnetization for the core contribution. The calculations (details can be found in the Supporting Information section) allow us to estimate a magnetization value of 116(3) emu/g for the shell layer, which is in agreement with other reports on Zn-substituted ferrites^{77,84,85} and can be understood in terms of the Zn occupancy in the shell⁸⁶. Given the strong antiferromagnetic interaction between cations in tetrahedral and octahedral sites, as Zn²⁺ atoms start occupying the tetrahedral sites the net magnetic moment between both sublattices is raised, increasing the overall magnetization. However, a further decrease is expected when the Zn content approaches 1, and pure ZnFe₂O₄ is indeed antiferromagnetic because the moments of Fe³⁺ cations are perfectly compensated in octahedral sites³². The Zn fraction close to 0.6 of our shell layer is then responsible for the large overall magnetization. At room temperature, the same calculation leads to a shell magnetization of 74(2) emu/g, indicating that the magnetization of the Zn-ferrite is strongly temperature-dependent, similar to a recent finding of Albino et al.⁸⁴. In sum, our results suggest that the Zn-ferrite, apart from preserving the Fe₃O₄ stoichiometry, provides an increased magnetization, which is a remarkable advantage compared to other non-magnetic coatings such as SiO₂ or MgO.

An estimation of the effective anisotropies according to the Stoner-Wohlfarth theory for randomly oriented NPs with uniaxial anisotropy (see the Supporting Information for more details) reveals that both bare cores and core/shell NPs present similar values around $1.8(1) \cdot 10^5$ erg/cm³ at 5 K and $1.4(2) \cdot 10^5$ erg/cm³ at room temperature. Such values can be compared to the low temperature uniaxial anisotropies observed for Fe₃O₄

($6 \cdot 10^5$ erg/cm³)⁸⁷ or Zn_{0.6}Fe_{2.4}O₄ ($1 \cdot 10^5$ erg/cm³)⁸⁵. While the reduction in the effective anisotropy of the core/shell sample compared to pure Fe₃O₄ is attributed to the contribution of the softer shell layer, in the case of the bare cores it should be ascribed to the presence of maghemite, whose magnetocrystalline anisotropy is around one-third of the magnetite value¹⁹. The above analysis highlights the importance of a careful characterization of the iron oxidation state in the NPs, as small variations in the effective anisotropy can result in strong changes in the functional properties, as typically observed e.g. in magnetic fluid hyperthermia^{88–90}. To further illustrate this point, we calculated the expected variation of the power losses due to the aging effect on the magnetic properties. Typical radiofrequency fields ($H_{MAX}=30-100$ Oe, $f=300$ kHz) were

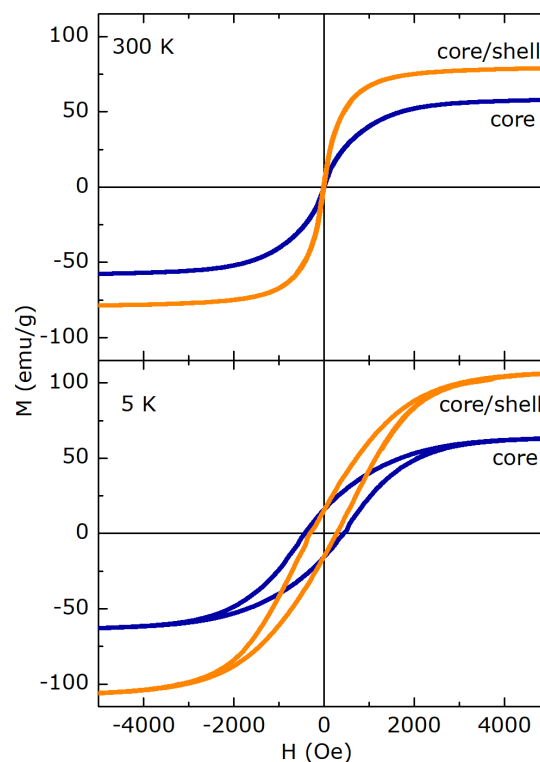


Figure 6 Hysteresis loops measured at 300 K (upper panel) and 5 K (lower panel) for the bare aged cores and core/shell NPs.

considered in the calculations and the hysteresis areas were simulated in the frame of the linear response theory⁸⁸ (full details are reported in the Supporting Information section). The results indicate that the power losses are strongly decreased for the aged bare cores compared to fresh stoichiometric Fe₃O₄ NPs due to the reduced M_s and K_{eff} . According to our simulations, apart from being less-dependent on the aging process, the core/shell NPs' hysteresis losses are also larger due to the fine-tuning of the size and magnetic properties, in agreement with previous experimental results⁴⁸. Although frequently overlooked in the study of hybrid core/shell NPs, the control of the surface chemistry of the iron oxide cores here is confirmed by a number of different experimental techniques. Our study also reveals that stoichiometric Fe₃O₄ is effectively obtained for fresh NPs prepared by Sun's method³³, without FeO or γ -Fe₂O₃ impurities. Therefore, it is likely that the maghemite-magnetite

mixtures previously observed by other authors in NPs prepared by the same method are actually a result of post-synthetic oxidation due to air exposure.

At this point we can briefly discuss some key points regarding the magnetite oxidation process. In the topotaxial low temperature oxidation of magnetite to maghemite oxygen ions are ionized at the surface of the NPs by the electrons arising from the oxidation of Fe^{2+} , while Fe cations migrate outwards to retain the charge neutrality in the material. Such process is typically described through the Fick's second law by assuming radial cation diffusion in spherical particles^{14,30,31}. Our experimental results confirm the presence of partly oxidized aged magnetite cores (55% $\gamma\text{-Fe}_2\text{O}_3$) and a preserved core stoichiometry for aged core/shell $\text{Fe}_3\text{O}_4/\text{Zn}_{0.6}\text{Fe}_{2.4}\text{O}_4$ NPs (<5 % $\gamma\text{-Fe}_2\text{O}_3$, taking the estimated errors of the Mössbauer analysis as an upper limit for the maghemite fraction). Assuming that the same transport mechanisms are operative in both cases, this implies that the effective cation diffusivities are lowered for the magnetite core in the core/shell sample. The experimental maghemite fractions in the aged samples allow to roughly estimate Fe diffusivity values of around $1 \times 10^{-25} \text{ m}^2/\text{s}$ for the bare cores and an upper bound of $5 \times 10^{-28} \text{ m}^2/\text{s}$ for the magnetite core in core/shell NPs (details of the calculations are shown in the Supporting Information section). The former is lower than the $4.5 \times 10^{-25} \text{ m}^2/\text{s}$ reported by Bogart et al. for $\approx 15 \text{ nm}$ uncoated Fe_3O_4 NPs prepared by a co-precipitation method and reflects that the good crystallinity of our bare cores, as well as the presence of the organic capping, may be contributing to decrease the cation diffusivity. In the core/shell sample, the lower electronic conductivity of the Zn ferrite layer^{19,91} provides a barrier for electron conduction responsible for a decrease in the Fe diffusivities, as observed in Zn, Co or Ni-substituted magnetites³⁰. At the same time, electron tunnelling is only operative for thicknesses below 2.5 nm ^{92,93}, suggesting that a minimum thickness is needed to retard the oxidation process and those larger than 3 nm would not be more advantageous in passivating the magnetite core. It is worth to mention that previous works suggest a particle structure formed by a magnetite core surrounded by a uniform maghemite layer and point to an oxidized shell in the same thickness range^{33,34}. In addition, the epitaxial growth of the shell layer revealed by the structural characterization should be playing an important role in slowing down the oxidation process by providing negligible epitaxial strain due to the excellent lattice and crystal symmetry match between Fe_3O_4 and $\text{Zn}_{0.6}\text{Fe}_{2.4}\text{O}_4$ crystal structures. In fact, it has been reported that the diffusion of cations is dramatically increased at grain boundaries or due to the presence of crystal defects^{37,94}, which are absent in our core/shell NPs. This fact could also explain the remarkable lack of Verwey transitions in silica-coated iron oxides^{43–46}, for which the amorphous nature and porosity of the SiO_2 could be facilitating both oxygen and ion transport across the shell layer⁹⁵, decreasing its efficiency to prevent the Fe_3O_4 oxidation.

Conclusions

The study of bare iron oxide cores and $\text{Fe}_3\text{O}_4/\text{Zn}_{0.6}\text{Fe}_{2.4}\text{O}_4$ core/shell NPs reveals the remarkable role of the Zn-ferrite shell in controlling the surface chemistry of magnetite cores. While X-ray photoelectron spectroscopy confirms that 6 month-aged magnetite nanoparticles are partially oxidized to maghemite, the $\text{Fe}_3\text{O}_4/\text{Zn}_{0.6}\text{Fe}_{2.4}\text{O}_4$ core/shell NPs exhibit a sharp Verwey transition that indicates the presence of a stoichiometric 12 nm Fe_3O_4 core even after the environmental aging, which is confirmed by Mössbauer and electron energy loss spectroscopies. Our results also suggest that Sun's thermal decomposition method for the synthesis of iron oxides provide highly stoichiometric magnetite NPs, while the partial oxidation shown in several reports is likely associated with a post-synthesis oxidation. As a result, the $\text{Fe}_3\text{O}_4/\text{Zn}_{0.6}\text{Fe}_{2.4}\text{O}_4$ core/shell NPs provide a chemically stable magnetite core with bulk-like properties while the Zn-ferrite shell provides an additional degree of freedom to control the overall magnetization and magnetic anisotropy. Indeed, the Zn-ferrite, in addition to preserving the Fe_3O_4 stoichiometry, is responsible for an increased magnetization. Finally, unlike other coating layers, such as SiO_2 , the epitaxial growth and the crystal symmetry match between the magnetite core and the Zn-ferrite provide an isolating non-defective shell that hinders the oxidation process of the Fe_3O_4 .

Conflicts of interest

There are no conflicts to declare.

Author contributions

G.C.L., M-H.P., H.S., C.V. and M.H.F. conceived the work and planned the experiments. A.R. performed and analyzed the XPS measurements. Y.X. performed and analyzed the STEM-EELS experiments. R.D. and J.R. performed the magnetic measurements. F.J.L. and E.B.-S. analyzed the Mössbauer data. G.C.L. synthesized the samples, performed the experiments and wrote the manuscript. All authors edited the manuscript.

Acknowledgements

The authors thank Consejo Nacional de Investigaciones Científicas y Técnicas (CONICET). GCL acknowledges CNPq and the Fulbright Commission for financial support, Dr. Alberto Caneiro from YTEC for assistance with the electron microscopy and Prof. Tatiana D. Saint Pierre and Rafael C. C. Rocha from PUC-Rio for the ICP-MS measurements. This work was supported in part by CONICET (PIP 0333 and 0093), ANPCyT (PICT 2017-4519), Universidad Nacional de La Plata (UNLP X786 and X760) of Argentina. YX gratefully acknowledges FAPERJ for the support with grant numbers E-26/010.000978/2019 and E-26/010.001550/2019. Research at USF was supported by the U.S. Department of Energy, Office of Basic Energy Sciences, Division of Materials Sciences and Engineering under Award No. DE-FG02-07ER46438.

Notes and references

- 1 N. Lee, D. Yoo, D. Ling, M. H. Cho, T. Hyeon and J. Cheon, *Chem. Rev.*, 2015, **115**, 10637–10689.
- 2 D. Ortega and Q. A. Pankhurst, 2013, vol. 1, pp. 60–88.
- 3 C. Grüttner, K. Müller, J. Teller and F. Westphal, *Int. J. Hyperth.*, 2013, **29**, 777–789.
- 4 Z. W. Tay, P. Chandrasekharan, A. Chiu-Lam, D. W. Hensley, R. Dhavalikar, X. Y. Zhou, E. Y. Yu, P. W. Goodwill, B. Zheng, C. Rinaldi and S. M. Conolly, *ACS Nano*, 2018, **12**, 3699–3713.
- 5 E. Guisasola, A. Baeza, L. Asín, J. M. de la Fuente and M. Vallet-Regí, *Small Methods*, 2018, **1800007**, 1800007.
- 6 H. Zeng, C. T. Black, R. L. Sandstrom, P. M. Rice, C. B. Murray and S. Sun, *Phys. Rev. B*, 2006, **73**, 020402.
- 7 J. Chen, X. Ye, S. J. Oh, J. M. Kikkawa, C. R. Kagan and C. B. Murray, *ACS Nano*, 2013, **7**, 1478–86.
- 8 B. H. Zhou and J. D. Rinehart, *ACS Appl. Electron. Mater.*, 2019, **1**, 1065–1069.
- 9 F. Fabris, E. Lima, C. Quinteros, L. Neñer, M. Granada, M. Sirena, R. D. Zysler, H. E. Troiani, V. Leborán, F. Rivadulla and E. L. Winkler, *Phys. Rev. Appl.*, 2019, **11**, 1.
- 10 T. Tsuchiya, K. Terabe, M. Ochi, T. Higuchi, M. Osada, Y. Yamashita, S. Ueda and M. Aono, *ACS Nano*, 2016, **10**, 1655–1661.
- 11 J.-B. Moussy, *J. Phys. D. Appl. Phys.*, 2013, **46**, 143001.
- 12 A. Bupathy, V. Banerjee and J. Carrey, *Phys. Rev. B*, 2019, **100**, 064420.
- 13 S. Chandra, R. Das, V. Kalappattil, T. Eggers, C. Harnagea, R. Nechache, M.-H. Phan, F. Rosei and H. Srikanth, *Nanoscale*, 2017, **9**, 7858–7867.
- 14 L. K. Bogart, C. Blanco-Andujar and Q. A. Pankhurst, *Appl. Phys. Lett.*, 2018, **113**, 133701.
- 15 E. Demangeat, M. Pédrot, A. Dia, M. Bouhnik-Le-Coz, F. Grasset, K. Hanna, M. Kamagate and F. Cabello-Hurtado, *Environ. Sci. Nano*, 2018, **5**, 992–1001.
- 16 S. P. Schwaminger, D. Bauer, P. Fraga-García, F. E. Wagner and S. Berensmeier, *CrystEngComm*, 2017, **19**, 246–255.
- 17 M.-H. Phan, J. Alonso, H. Khurshid, P. Lampen-Kelley, S. Chandra, K. Stojak Repa, Z. Nemati, R. Das, Ó. Iglesias and H. Srikanth, *Nanomaterials*, 2016, **6**, 221.
- 18 A. G. Roca, J. F. Marco, M. Del Puerto Morales and C. J. Serna, *J. Phys. Chem. C*, 2007, **111**, 18577–18584.
- 19 J. M. D. Coey, *Magnetism and magnetic materials*, Cambridge University Press, 2010.
- 20 J. P. Kehrer, *Toxicology*, 2000, **149**, 43–50.
- 21 L. Gao, J. Zhuang, L. Nie, J. Zhang, Y. Zhang, N. Gu, T. Wang, J. Feng, D. Yang, S. Perrett and X. Yan, *Nat. Nanotechnol.*, 2007, **2**, 577–583.
- 22 T. Kang, Y. G. Kim, D. Kim and T. Hyeon, *Coord. Chem. Rev.*, 2020, **403**, 1–21.
- 23 L. Gao, K. Fan and X. Yan, *Theranostics*, 2017, **7**, 3207–3227.
- 24 J. García and G. Subías, *J. Phys. Condens. Matter*, 2004, **16**, R145–R178.
- 25 X. H. Liu, a. D. Rata, C. F. Chang, a. C. Komarek and L. H. Tjeng, *Phys. Rev. B*, 2014, **90**, 125142.
- 26 E. Lima, G. E. S. Brito, C. Cavalius, V. Sivakov, H. Shen, S. Mathur and G. F. Goya, *Curr. Nanosci.*, 2012, **8**, 659–668.
- 27 J. Santoyo Salazar, L. Perez, O. De Abril, L. Truong Phuoc, D. Ihiawakrim, M. Vazquez, J. M. Greneche, S. Begin-Colin and G. Pourroy, *Chem. Mater.*, 2011, **23**, 1379–1386.
- 28 J. Lee, S. G. Kwon, J.-G. Park and T. Hyeon, *Nano Lett.*, 2015, **15**, 4337–4342.
- 29 R. M. Cornell and U. Schwertmann, *The Iron Oxides: Structure, Properties, Reactions, Occurrences and Uses*, Wiley-VCH, Weinheim, 2nd edn., 2003.
- 30 P. S. Sidhu, R. J. Gilkes and A. M. Posner, *J. Inorg. Nucl. Chem.*, 1977, **39**, 1953–1958.
- 31 J. Tang, M. Myers, K. A. Bosnick and L. E. Brus, *J. Phys. Chem. B*, 2003, **107**, 7501–7506.
- 32 B. D. Cullity and C. D. Graham, *Introduction to magnetic materials*, John Wiley & Sons, New Jersey, 2nd edn., 2009.
- 33 H. Sharifi Dehsari, V. Ksenofontov, A. Möller, G. Jakob and K. Asadi, *J. Phys. Chem. C*, 2018, **122**, 28292–28301.
- 34 R. Frison, G. Cernuto, A. Cervellino, O. Zaharko, G. M. Colonna, A. Guagliardi and N. Masciocchi, *Chem. Mater.*, 2013, **25**, 4820–4827.
- 35 K. Yuan, S. S. Lee, W. Cha, A. Ulvestad, H. Kim, B. Abdilla, N. C. Sturchio and P. Fenter, *Nat. Commun.*, 2019, **10**, 1–10.
- 36 G. M. da Costa, C. Blanco-Andujar, E. De Grave and Q. a Pankhurst, *J. Phys. Chem. B*, 2014, **118**, 11738–11746.
- 37 A. Pratt, L. Lari, O. Hovorka, A. Shah, C. Woffinden, S. P. Tear, C. Binns and R. Kröger, *Nat. Mater.*, 2014, **13**, 26–30.
- 38 A. Fraile Rodríguez, C. Moya, M. Escoda-Torroella, A. Romero, A. Labarta and X. Batlle, *J. Mater. Chem. C*, 2018, **6**, 875–882.
- 39 T. P. Almeida, T. Kasama, A. R. Muxworthy, W. Williams, L. Nagy, T. W. Hansen, P. D. Brown and R. E. Dunin-Borkowski, *Nat. Commun.*, 2014, **5**, 1–6.
- 40 L. Wu, A. Mendoza-García, Q. Li and S. Sun, *Chem. Rev.*, 2016, **116**, 10473–10512.
- 41 J. A. De Toro, M. Vasilakaki, S. S. Lee, M. S. Andersson, P. S. Normile, N. Yaacoub, P. Murray, E. H. Sánchez, P. Muñoz, D. Peddis, R. Mathieu, K. Liu, J. Geshev, K. N. Trohidou and J. Nogués, *Chem. Mater.*, 2017, **29**, 8258–8268.
- 42 P. C. Rivas Rojas, P. Tancredi, O. Moscoso Londoño, M. Knobel and L. M. Socolovsky, *J. Magn. Magn. Mater.*, 2018, **451**, 688–696.
- 43 N. Pérez, C. Moya, P. Tartaj, A. Labarta and X. Batlle, *J. Appl. Phys.*, 2017, **121**, 044304.
- 44 E. S. D. T. de Mendonça, A. C. B. de Faria, S. C. L. Dias, F. F. H. Aragón, J. C. Mantilla, J. A. H. Coaquira and J. A. Dias, *Surfaces and Interfaces*, 2019, **14**, 34–43.
- 45 C. Schmitz-Antoniak, D. Schmitz, A. Warland, M. Darbandi, S. Haldar, S. Bhandary, B. Sanyal, O. Eriksson and H. Wende, *Ann. Phys.*, 2018, **530**, 1–7.
- 46 S. Larumbe, C. Gómez-Polo, J. I. Pérez-Landazábal and J. M. Pastor, *J. Phys. Condens. Matter*, 2012, **24**, 266007.
- 47 H. L. Ding, Y. X. Zhang, S. Wang, J. M. Xu, S. C. Xu and G. H. Li, *Chem. Mater.*, 2012, **24**, 4572–4580.
- 48 G. C. Lavorato, R. Das, Y. Xing, J. Robles, F. J. Litterst, E. Baggio-Saitovitch, M. Phan and H. Srikanth, *ACS Appl. Nano Mater.*, 2020, **3**, 1755–1765.

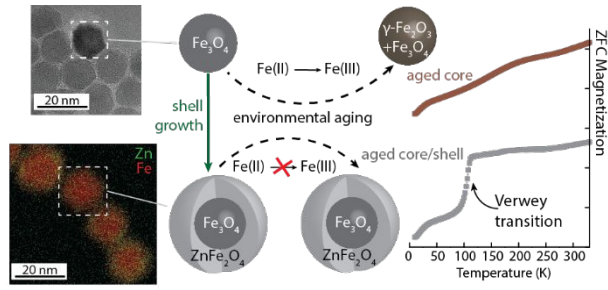
- 49 S. Sun, H. Zeng, D. B. Robinson, S. Raoux, P. M. Rice, S. X. Wang and G. Li, *J. Am. Chem. Soc.*, 2004, **126**, 273–9.
- 50 Z. Nedelkoski, D. Kepaptsoglou, L. Lari, T. Wen, R. A. Booth, S. D. Oberdick, P. L. Galindo, Q. M. Ramasse, R. F. L. Evans, S. Majetich and V. K. Lazarov, *Sci. Rep.*, 2017, **7**, 45997.
- 51 F. Crippa, L. Rodriguez-Lorenzo, X. Hua, B. Goris, S. Bals, J. S. Garitaonandia, S. Balog, D. Burnand, A. M. Hirt, L. Haeni, M. Lattuada, B. Rothen-Rutishauser and A. Petri-Fink, *ACS Appl. Nano Mater.*, 2019, **2**, 4462–4470.
- 52 G. Lavorato, M. Alzamora, C. Contreras, G. Burlandy, F. J. Litterst and E. Baggio-Saitovitch, *Part. Part. Syst. Charact.*, 2019, **36**, 1900061.
- 53 D. Lachowicz, R. Wirecka, W. Górka-Kumik, M. M. Marzec, M. Gajewska, A. Kmita, J. Żukrowski, M. Sikora, S. Zapotoczny and A. Bernasik, *Phys. Chem. Chem. Phys.*, 2019, **21**, 23473–23484.
- 54 D. Wilson and M. A. Langell, *Appl. Surf. Sci.*, 2014, **303**, 6–13.
- 55 L. Zhang, R. He and H. C. Gu, *Appl. Surf. Sci.*, 2006, **253**, 2611–2617.
- 56 M. Doig, C. P. Warrens and P. J. Camp, *Langmuir*, 2014, **30**, 186–195.
- 57 A. Dreyer, A. Feld, A. Kornowski, E. D. Yilmaz, H. Noei, A. Meyer, T. Krekeler, C. Jiao, A. Stierle, V. Abetz, H. Weller and G. A. Schneider, *Nat. Mater.*, 2016, **15**, 522–528.
- 58 G. C. Lavorato, E. Lima Jr, D. Tobia, D. Fiorani, H. E. Troiani, R. D. Zysler and E. L. Winkler, *Nanotechnology*, 2014, **25**, 355704.
- 59 J. Schindelin, I. Arganda-Carreras, E. Frise, V. Kaynig, M. Longair, T. Pietzsch, S. Preibisch, C. Rueden, S. Saalfeld, B. Schmid, J.-Y. Tinevez, D. J. White, V. Hartenstein, K. Eliceiri, P. Tomancak and A. Cardona, *Nat. Methods*, 2012, **9**, 676–682.
- 60 J. Wan, X. Jiang, H. Li and K. Chen, *J. Mater. Chem.*, 2012, **22**, 13500.
- 61 L. Qiao, Z. Fu, J. Li, J. Ghosen, M. Zeng, J. Stebbins, P. N. Prasad and M. T. Swihart, *ACS Nano*, 2017, **11**, 6370–6381.
- 62 M. C. Biesinger, B. P. Payne, A. P. Grosvenor, L. W. M. Lau, A. R. Gerson and R. S. C. Smart, *Appl. Surf. Sci.*, 2011, **257**, 2717–2730.
- 63 D. Wilson and M. A. Langell, *Appl. Surf. Sci.*, 2014, **303**, 6–13.
- 64 S. Poulin, R. França, L. Moreau-Bélanger and E. Sacher, *J. Phys. Chem. C*, 2010, **114**, 10711–10718.
- 65 B. D. Cullity and S. R. Stock, *Elements of X-ray Diffraction*, Prentice hall New Jersey, 2001, vol. 3.
- 66 P. Torruella, R. Arenal, F. De La Peña, Z. Saghi, L. Yedra, A. Eljarrat, L. López-Conesa, M. Estrader, A. López-Ortega, G. Salazar-Alvarez, J. Nogués, C. Ducati, P. A. Midgley, F. Peiró and S. Estradé, *Nano Lett.*, 2016, **16**, 5068–5073.
- 67 C. Colliex, T. Manoubi and C. Ortiz, *Phys. Rev. B*, 1991, **44**, 11402–11411.
- 68 L. Cavé, T. Al, D. Loomer, S. Cogswell and L. Weaver, *Micron*, 2006, **37**, 301–309.
- 69 C. Colliex, T. Manoubi and C. Ortiz, *Phys. Rev. B*, 1991, **44**, 11402–11411.
- 70 G. A. Sawatzky, *Phys. Rev.*, 1969, **183**, 383–386.
- 71 I. Dézsi, C. Fetzer, Á. Gombkötő, I. Szűcs, J. Gubicza and T. Ungár, *J. Appl. Phys.*, 2008, **103**, 104312.
- 72 J. Fock, L. K. Bogart, D. González-Alonso, J. I. Espeso, M. F. Hansen, M. Varón, C. Frandsen and Q. A. Pankhurst, *J. Phys. D: Appl. Phys.*, 2017, **50**, 265005.
- 73 I. Dézsi, C. Fetzer, Á. Gombkötő, I. Szűcs, J. Gubicza and T. Ungár, *J. Appl. Phys.*, 2008, **103**, 104312.
- 74 E. J. W. Verwey and E. L. Heilmann, *J. Chem. Phys.*, 1947, **15**, 174–180.
- 75 J. Smit and H. P. J. Wijn, *Adv. Electron. Electron Phys.*, 1954, **6**, 69–136.
- 76 G. A. Petitt and D. W. Forester, *Phys. Rev. B*, 1971, **4**, 3912–3923.
- 77 V. Mameli, A. Musinu, A. Ardu, G. Ennas, D. Peddis, D. Niznansky, C. Sangregorio, C. Innocenti, N. T. K. Thanh and C. Cannas, *Nanoscale*, 2016, **8**, 10124–10137.
- 78 X. Liu, J. Liu, S. Zhang, Z. Nan and Q. Shi, *J. Phys. Chem. C*, 2016, **120**, 1328–1341.
- 79 G. C. Lavorato, E. Lima, H. E. Troiani, R. D. Zysler and E. L. Winkler, *Nanoscale*, 2017, **9**, 10240–10247.
- 80 E. Ferreira-Vila, L. Iglesias, I. Lucas del Pozo, N. Varela-Dominguez, C. T. Bui, B. Rivas-Murias, J. M. Vila-Fungueiriño, P. Jimenez-Cavero, C. Magen, L. Morellon, V. Pardo and F. Rivadulla, *APL Mater.*, 2019, **7**, 031109.
- 81 G. Lavorato, E. Winkler, B. Rivas-Murias and F. Rivadulla, *Phys. Rev. B*, 2016, **94**, 054405.
- 82 X. Liu, C.-F. Chang, A. D. Rata, A. C. Komarek and L. H. Tjeng, *npj Quantum Mater.*, 2016, **1**, 16027.
- 83 Q. Song and Z. J. Zhang, *J. Am. Chem. Soc.*, 2012, **134**, 10182–90.
- 84 M. Albino, E. Fantechi, C. Innocenti, A. López-Ortega, V. Bonanni, G. Campo, F. Pineider, M. Gurioli, P. Arosio, T. Orlando, G. Bertoni, C. de Julián Fernández, A. Lascialfari and C. Sangregorio, *J. Phys. Chem. C*, 2019, **123**, 6148–6157.
- 85 S. He, H. Zhang, Y. Liu, F. Sun, X. Yu, X. Li, L. Zhang, L. Wang, K. Mao, G. Wang, Y. Lin, Z. Han, R. Sabirianov and H. Zeng, *Small*, 2018, **14**, 1800135.
- 86 N. Modaresi, R. Afzalzadeh, B. Aslibeiki, P. Kameli, A. Ghotbi Varzaneh, I. Orue and V. A. Chernenko, *J. Magn. Magn. Mater.*, 2019, **482**, 206–218.
- 87 M. Ziese, R. Höhne, P. Esquinazi and P. Busch, *Phys. Rev. B*, 2002, **66**, 134408.
- 88 J. Carrey, B. Mehdaoui and M. Respaud, *J. Appl. Phys.*, 2011, **109**, 083921.
- 89 E. Lima, E. De Biasi, R. D. Zysler, M. Vasquez Mansilla, M. L. Mojica-Pisciotti, T. E. Torres, M. P. Calatayud, C. Marquina, M. Ricardo Ibarra and G. F. Goya, *J. Nanoparticle Res.*, 2014, **16**, 2791.
- 90 D. Lachowicz, W. Górka, A. Kmita, A. Bernasik, J. Zukrowski, W. Szczerba, M. Sikora, C. Kapusta and S. Zapotoczny, *J. Mater. Chem. B*, 2019, **7**, 2962–2973.
- 91 J. Takaobushi, H. Tanaka, T. Kawai, S. Ueda, J.-J. Kim, M. Kobata, E. Ikenaga, M. Yabashi, K. Kobayashi, Y. Nishino, D. Miwa, K. Tamasaku and T. Ishikawa, *Appl. Phys. Lett.*, 2006, **89**, 242507.
- 92 A. Cabot, V. F. Puentes, E. Shevchenko, Y. Yin, L. Balcells, M.

Journal Name

ARTICLE

- A. Marcus, S. M. Hughes and A. P. Alivisatos, *J. Am. Chem. Soc.*, 2007, **129**, 10358–10360.
- 93 A. Atkinson, *Rev. Mod. Phys.*, 1985, **57**, 437–470.
- 94 F. Bourgeois, P. Gergaud, H. Renevier, C. Leclere and G. Feuillet, *J. Appl. Phys.*, 2013, **113**, 013510.
- 95 E. A. Schultz-Sikma, H. M. Joshi, Q. Ma, K. W. MacRenaris, A. L. Eckermann, V. P. Dravid and T. J. Meade, *Chem. Mater.*, 2011, **23**, 2657–2664.

Table of Contents Graphics



Magnetite nanostructures gradually oxidize under environmental conditions, leading to changes in their magnetic response. Here we demonstrate that a Zn-ferrite epitaxial coating protects magnetite nanoparticles from oxidation and provides a core/shell system with enhanced magnetic properties.